Harnessing Acoustic Energy with Liquid Metal Triboelectric Nanogenerators: A Promising Approach for Moving-Parts-Free Power Generation

Fawad Ahmed,[1†] Junxiang Wang,[1,5†] Rui Yang,[1*] Guoyao Yu,[1,2] Shunmin Zhu,[4] Wei Tang,[3*] Ercang Luo,[1,5*]

[1]CAS Key Laboratory of Cryogenics, Technical Institute of Physics and Chemistry, Chinese Academy of Sciences, Beijing 100190, China

[2]Institute of Optical Physics and Engineering Technology, Qilu Zhongke, Jinan 251000, China

[3]CAS Center for Excellence in Nanoscience, Beijing Key Laboratory of Micro-nano Energy and Sensor, Beijing Institute of Nanoenergy and Nanosystems, Chinese Academy of Sciences, Beijing 101400, China

[4]Department of Engineering, Durham University, Durham DH1 3LE, UK

[5]University of Chinese Academy of Sciences, Beijing 100049, China

Abstract

Heat-driven acoustic engines (HDAEs) offer a promising approach to energy generation without solid moving parts. However, integrating linear alternators for acoustic-to-electric conversion introduces moving components, diminishing this advantage. To tackle this issue, we investigate using an acoustically-driven liquid-metal triboelectric generator (LM-TEG) within HDAEs for acoustic-to-electric conversion. Experiments were conducted in three settings: mechanically-driven LM-TEGs under atmospheric and pressurized gas conditions, and acoustically-driven LM-TEGs. Results from mechanically-driven LM-TEG tests show that using FEP material, increasing LM-TEG contact area, stacking TEGs in parallel, and using pressurized gas enhance performance. Acoustically-driven LM-TEG experiments demonstrate significant improvements with pressurized nitrogen, achieving a short-circuit current approximately 4.5 times higher than with helium at equivalent pressures. Notably, charge and power densities reached 388 μC/m² and 1.7 W/m², respectively, surpassing typical values from conventional TEGs. Importantly, these results were obtained with a complete, fully integrated acoustically driven LM-TEG system. This study represents the first investigation in the literature of acoustically driven LM-TEGs, offering a

† These authors contributed equally to this work.
* Authors to whom correspondence should be addressed yangrui@mail.ipc.ac.cn, tangwei@binn.cas.cn, ecluo@mail.ipc.ac.cn

distinct power generation system with no solid moving parts. The findings validate the feasibility of integrating LM-TEGs with HDAEs and suggest their potential for large-scale power generation, moving beyond the small-scale applications that have dominated prior TEG research.

Keywords

Acoustics, Triboelectric Generator, Liquid Metal, Equivalent Circuit Model, Finite Element Method, Power Generation.

1. Introduction

The quest for sustainable and efficient power generation systems has driven researchers to explore innovative approaches that challenge the limitations of traditional technologies. One such promising avenue lies at the intersection of acoustics and Triboelectric Generators (TEGs), particularly the liquid metal-based TEGs, where the potential for acoustic-to-electric conversion holds the key to a frictionless future of power generation. As the global energy demand continues to rise [1], the need for clean, reliable, and cost-effective power generation solutions has become increasingly pressing [2]. Conventional power generation systems often rely on solid-state components and moving parts, which can be susceptible to wear, friction, and mechanical failure, limiting their long-term efficiency and sustainability.

Heat-driven acoustic engine (HDAE or TAHE) presents a promising path for sustainable power generation by harnessing clean energy sources like solar, waste heat, geothermal, and biomass [3]. These systems leverage the interaction between acoustic waves and solid boundaries to drive thermodynamic cycles. HDAE can be broadly classified into two main categories: standing wave and traveling wave TAHEs. Standing wave engines use a simple stack-based design, providing reliability and ease of construction. However, the inherent heat transfer irreversibility limits their thermal efficiency to around 20% [4]. On the other hand, traveling wave TAHEs are more complex regenerator-based engines known for their high efficiency [5], [6] (efficiency above 30%, compatible with Internal Combustion (IC) engines). Recent studies have enhanced standing-wave TAHE performance through external velocity perturbations [7] and geometric optimizations such as tapered conical resonators [8], improving acoustic power output and efficiency. These advancements aim to make standing-wave TAHEs more competitive with their traveling wave counterparts.

HDAEs offer a transformative approach to energy conversion, leveraging the power of acoustic waves instead of conventional mechanical components [9]. This technology harnesses controlled acoustic waves to drive the compression, expansion, and displacement of the working gas, eliminating the need for pistons, valves, and seals. This innovative design offers a significant advantage over traditional energy generation systems - the absence of moving parts. This translates to reduced mechanical friction and wear, leading to a longer lifespan and lower maintenance requirements [10], [11]. In a typical heat-driven acoustic power generation system (HDAPGS), there are two conversion mechanisms: the transformation of thermal energy into acoustic energy, followed by the conversion of acoustic energy into electrical energy [12]. While effective, the use of resonant linear alternators to convert the generated acoustic power into electricity introduces moving parts into the system, compromising one of the key benefits of an HDAGS. To fully unlock the potential of this technology and maintain its edge over conventional systems, the development of novel acoustic-to-electric conversion solutions that eliminate moving parts is crucial. Exploring alternative approaches such as piezoelectric transducers, magnetohydrodynamic converters and triboelectric generators (TEGs/TENGs) holds significant promise for achieving this goal. Piezoelectric transducers are well suited for miniaturized, high-frequency HDAEs [13], [14] and are rendered inefficient for large-scale applications [15]. While theoretical predictions and performance calculations for MHD generators in Heat-driven acoustic power generation are promising, there is limited experimental work to confirm these calculation results. Besides the use of heavy magnets in the MHD prototypes introduces extra design challenges [16], [17], [18].

TENGs, on the other hand, offer distinct advantages in terms of simplicity, reliability, efficiency, scalability, cost-effectiveness, and environmental impact. Recently, considerable gains have been made in the performance enhancement of TENGs, with one study showing an exceptionally high instantaneous power density reaching up to 10 MW/(m^2) [19] and another reporting 85% [20] mechanical to electric conversion efficiency. Recent studies have demonstrated significant progress in TENG-based acoustic energy harvesting. A 3D-printed acoustic TENG with a quarter-wavelength resonator achieved 4.33 mW output under 100 dB excitation [21]. Additionally, a micro triboelectric ultrasonic device with a 50 μm-sized diaphragm enabled operation at megahertz frequencies [22]. These advancements highlight the

potential of TENGs for efficient acoustic energy conversion across various scales and frequencies, from low-frequency ambient noise to ultrasonic applications.

Invented in 2012, TENGs work by combining contact electrification and electrostatic induction [23] to convert mechanical energy into electric power [24], [25], [26]. Due to electron transfer, the triboelectric effect involves two materials becoming charged when separated after contact. Maxwell's displacement current drives the process [27]. Typically, TENGs operate in four modes: contact-separation mode [28], sliding mode [29], free-standing mode [30], and single-electrode mode [31]. TENGs are excellent at converting irregular, low-frequency, and low-amplitude mechanical energy into electric power, making them ideal for harvesting acoustic energy from HDAEs. The underlying concept is that a HDAE first converts thermal energy into acoustic power which is then intercepted by a triboelectric generator to convert directly into electricity [32], [33].

Typically, the solid-solid contact TENGs are used for various applications. However, the roughness of the two surfaces and their mutual roughness matching significantly influences the contact effect. Additionally, solid-to-solid contact generates friction and dissipates heat. These factors considerably restrict the efficiency and output power of the solid-solid contact TENG. According to a prominent experimental investigation by Tang et al. [34], replacing a traditional solid material with a liquid metal results in a liquid-solid contact TENG. This innovation offers advantages such as an enlarged liquid-solid contact area, a closely bound contact, and a smaller friction coefficient than a conventional solid-solid contact TENG. Thus, this innovation enables breakthroughs in high charge density and conversion efficiency. Experimental results indicated a maximum charge density of 430 $\mu C/m^2$, significantly surpassing the low [35], [36], [37], [38], [39], [40] (~ 100 $\mu C/m^2$) charge density observed in traditional solid-solid contact TENGs. Furthermore, the instantaneous energy conversion efficiency reached an impressive 70.6%.

Introducing a liquid column into a pure gas HDAPGS to form a gas-liquid coupled oscillating system can fully utilize the gas-working medium's compressibility and the liquid-working medium's inertia [41]. This approach effectively enhances acoustic oscillation and simultaneously reduces the system's resonant frequency [42]. Inspired by this concept, to further improve the reliability and output performance of the HDAE-driven LM-TEG, this work proposes and investigates a new coupling configuration between a sliding liquid-metal-based TEG and an acoustically-driven gas-liquid

resonance system. Based on thermal and acoustic theory, we systematically calculated the operational characteristics of the acoustically driven gas-liquid resonance system and the theoretical output characteristics of the sliding LM-TEG. Building upon theoretical calculations, we also conducted experimental research to examine the effects of introducing the LM-TEG and the acoustically driven gas-liquid resonance system on improving the coupled system's output.

In summary, while existing research in the fields of HDAPGS and TENG has made significant strides in energy conversion, a gap remains in exploring the intersection of these disciplines. This research investigates the feasibility of integrating acoustically-driven liquid metal triboelectric generators (LM-TEG) into HDAPGS for acoustic-to-electric conversion. The experimental results have demonstrated that an acoustic wave, exhibiting a frequency as low as 1 Hz, can be converted into an electric current of 7 μA when intercepted by an LM-TEG setup with a contact area of 30 cm^2. Furthermore, the acoustically-driven LM-TEG was able to achieve a remarkably high charge density of 388 $\mu C/m^2$. These findings highlight the significant potential of LM-TEGs to outperform conventional solid-solid contact TENG. By examining the operational characteristics of LM-TEG in different settings, this study seeks to contribute to the development of an innovative power generation system with no solid moving parts.

1.1 Working principle of a liquid metal triboelectric generator (LM-TEG)

The LM-TEG consists of two main parts: a liquid metal component and a TEG component, as shown in Fig. 1(a). The most commonly used liquid metals for LM-TEG are Mercury (Hg), Gallium (Ga), and Galinstan (an alloy of gallium, indium, and tin). However, both Ga and Galinstan are prone to instant oxidation, which adversely affects the performance of LM-TEG. Therefore, mercury was chosen as the liquid metal because it does not readily oxidize in the atmosphere, unlike Ga and Galinstan. The TEG component consists of two different materials: an electrode and a friction (also known as dielectric) material. In Fig. 1(a), fluorinated ethylene propylene (FEP) acts as the friction material while copper (Cu) as the electrode material.

The working principle of a single liquid metal-based TEG is illustrated in Fig. 1(b). When a dielectric material (FEP in this case) is fully submerged in liquid metal, the difference in electron affinity between the dielectric material and the liquid metal leads to the transfer of electrons from the liquid metal to the outer surface of the dielectric material, resulting in a negative charge on the dielectric material's outer

surface. The interface between the liquid metal and the dielectric material in contact becomes positively charged, as shown in Fig. 1b(i).

As the liquid level of the liquid metal column decreases, frictional charges are separated at the interface region, causing the potential of the liquid metal to be higher than that of the induced electrode. This leads to electrons flowing from the copper foil into the liquid metal through an external load, creating a reverse current, as depicted in Fig. 1b(ii). This process continues until the liquid metal column's liquid level is wholly separated from the dielectric material. At this point, the induced potential difference and transferred charge between the copper foil and the liquid metal reach their maximum values, as shown in Fig. 1b(iii).

When the liquid level of the liquid metal column begins to rise, the potential difference between the copper foil and the liquid metal decreases as the wetting area of the dielectric material increases. Consequently, electrons flow in the opposite direction from the liquid metal back to the copper foil, generating a current pattern as illustrated in Fig. 1b(iv). When the dielectric material is fully submerged in the liquid metal, the potential difference between the copper foil and the liquid metal disappears entirely, resulting in no charge transfer between them, as shown in Fig. 1b(i).

Thus, as the liquid metal column's liquid level undergoes reciprocating motion driven by acoustic waves, the LM-TEG generates a stable alternating current (AC) pulse output.

Fig. 1: Schematic of the working principle of liquid metal triboelectric generator (LM-TEG).

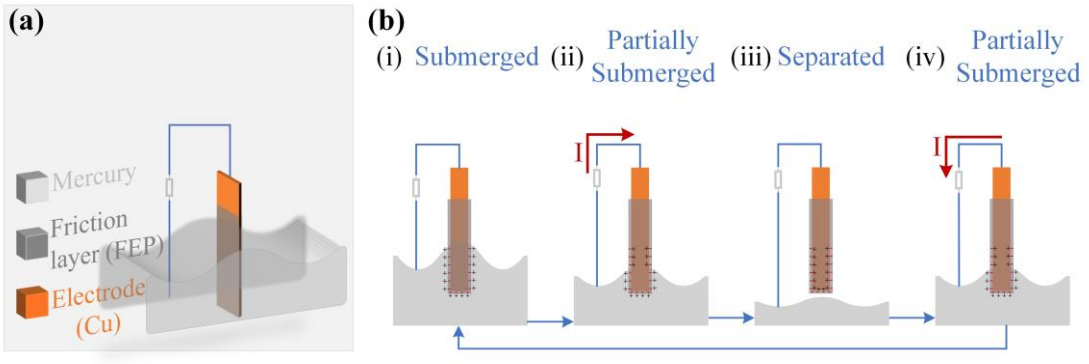

(a), **(b)** Schematic illustrating the working principle of a liquid metal triboelectric generator (LM-TEG).

2. Methods

2.1 Modeling methodology of the Standalone LM-TEG

In Fig. 1a, b, the Triboelectric Generator (TEG) operates in an electrode-dielectric sliding mode. This system utilizes FEP as the dielectric material and mercury (Hg) liquid metal, which serves the dual purpose of electrode and triboelectric surface. The charge density on the Hg surface is determined by the net difference between the triboelectric charges (σS) and the charges that are transferred ($\pm Q$), effectively making it $\sigma S \pm Q$. The dielectric layer has a thickness denoted by t_d and possesses a specific dielectric constant represented by ε_r. The mechanical motion modifies the gap (x) between the dielectrics, generating an electrical potential difference between the electrodes. This variation occurs as the active FEP layer slides in and out of the Hg, in accordance with the principles of the Gauss theorem. This theorem establishes that the total electric flux through a closed surface equals the enclosed charge over the permittivity. Consequently, the open circuit voltage equation for the sliding mode TEG is given as follows [29],

$$V_{oc} = \frac{\sigma d_0 x(t)}{\varepsilon_0 (l - x)} \tag{1}$$

A TEG operates similarly to a capacitor. In an electrode-dielectric sliding mode, a dielectric layer (FEP) is placed amongst the electrodes. This layer serves to insulate the electrodes (Hg and Cu), preventing direct contact between them. The presence of the dielectric layer increases the overall capacitance of the triboelectric generator (TEG), consequently lowering the intensity of the electric field and generating the necessary voltage for charging. The capacitance of the TEG, is calculated by:

$$C_{TENG} = \frac{\varepsilon_0 w (l - x(t))}{d_0} \tag{2}$$

d_0 is determined as follows,

$$d_0 = \frac{t_d}{\varepsilon_r} \tag{3}$$

Here, ε_0 is the free space and ε_r is relative permittivity, t_d is dielectric thickness, and w is width, while $x(t)$ is the time-dependent sliding distance. Finally, the modified charge equation which is implemented in the circuit model as follows,

$$Q = x * \left\{ \frac{\varepsilon_0 w (l - V(x(t))}{\left({}^{t_d}/_{\varepsilon_r} \right)} \right\} \tag{4}$$

Further details on the equivalent circuit model and FEM model implementations are provided in the supplementary information.

2.2 Experimental measurement methodology of LM-TEG's characteristics

The output charge, current, and voltage signals of the LM-TEG are measured using the Keithley 6517B electrometer/high-resistance meter. (See Fig. S4 in supplementary information). It is a sophisticated electrical measurement instrument designed for high-precision and low-current measurements in various scientific and industrial applications. The output signal from the Keithley 6517B is read and displayed on the computer in the LabVIEW (Laboratory Virtual Instrument Engineering Workbench) software by a National Instruments NI PXI-1033 chassis. The chassis hosts a PS PXI-3342 module, which contains eight analog input channels, each with a 24-bit resolution. The 6517B device is connected to one of the module's eight input channels to read the signal. In the initial stage of our experiment, we first devised a standalone system wherein a 24 V DC motor, with a maximum of 1000 rpm, is used to generate a reciprocating motion for the TEG to immerse in and separate from the mercury.

3. Results and discussion

We conducted three sets of experiments involving LM-TEG to achieve specific research goals. The first experiment examined a standalone, mechanically driven LM-TEG in a standard atmosphere to understand the characteristics of LM-TEG and optimize its performance. Secondly, we investigated the performance of LM-TEG in a pressurized gas environment to understand the influence of gas type and gas pressure on LM-TEG performance. This research is crucial as our ultimate goal is to integrate LM-TEG into a heat driven acoustic power generator, which operates in a high-pressure gas environment. Understanding the effects of gas type and pressure on LM-TEG performance is essential for this integration. Lastly, we conducted experiments involving an acoustically driven LM-TEG. In these experiments, acoustic waves were generated in a pressurized gas environment using a dual-opposed linear motor. The generated acoustic waves were intercepted by an LM-TEG set up in the system and converted to electrical energy. This experiment aimed to fully understand the acoustic-to-electric conversion mechanism for potential application in heat-driven acoustic power generators, where acoustic waves play a central role in energy conversion.

3.1 Modeling results of the Standalone LM-TEG

To estimate the electrical output performance of the LM-TEG, an equivalent circuit model of the LM-TEG was developed, as shown in Fig. 2a. The implementation methodology is enunciated in the methods section. The LM-TEG's electrical characteristics were evaluated at a sliding velocity of 0.25 m/s. For TEG, FEP (with a thickness of 50 μm) was employed as the dielectric material, copper served as the induction electrode, and mercury was used as the liquid metal. The results of this evaluation, encompassing the open-circuit voltage (V_{oc}), and short-circuit current (I_{sc}) are shown in Fig. 2b. The output current was monitored with different resistances connected in the load, exhibiting stability below 10 MΩ and gradually declining as resistance values increased. The peak output power reaches 2.2 mW at a resistance of 100 MΩ, equivalent to a power density of 1.5 W/m². Whereas the open circuit voltage peaked at 730 V, as illustrated in Fig. 2b.

Fig. 2c provides an estimate of the energy and charge produced by the LM-TEG. A maximum electrical energy of 1.15 mJ is produced at an optimal resistance of 100 MΩ. While a total of 425 nC charge is produced. Considering the 15 cm² contacting area of LM-TEG, the output charge density reached a substantial 283 μC/m², significantly surpassing the charge density typically achieved through solid-to-solid contact methods, which averages around 100 μC/(m²) [35], [36].

In order to compare the outcomes of the equivalent circuit model with those of the Finite Element Method (FEM) model, we utilized the COMSOL tool for modeling the LM-TEG. Specifically, we employed COMSOL's electrostatic module to execute the FEM simulation in the sliding mode. The results, as illustrated in Fig. 2d, unveil that the LM-TEG produced a maximum open circuit voltage of 800 V, resulting from the sliding motion of the TEG within the mercury medium. This is in good agreement with the 730 V prediction of the equivalent circuit model. The minor discrepancy between the two models' open circuit voltages is due to the presence of the load resistance in the circuit model and is therefore, unlike the FEM model, not fully an open circuit.

Fig. 2: Modeling results of standalone Liquid metal triboelectric generator (LM-TEG)

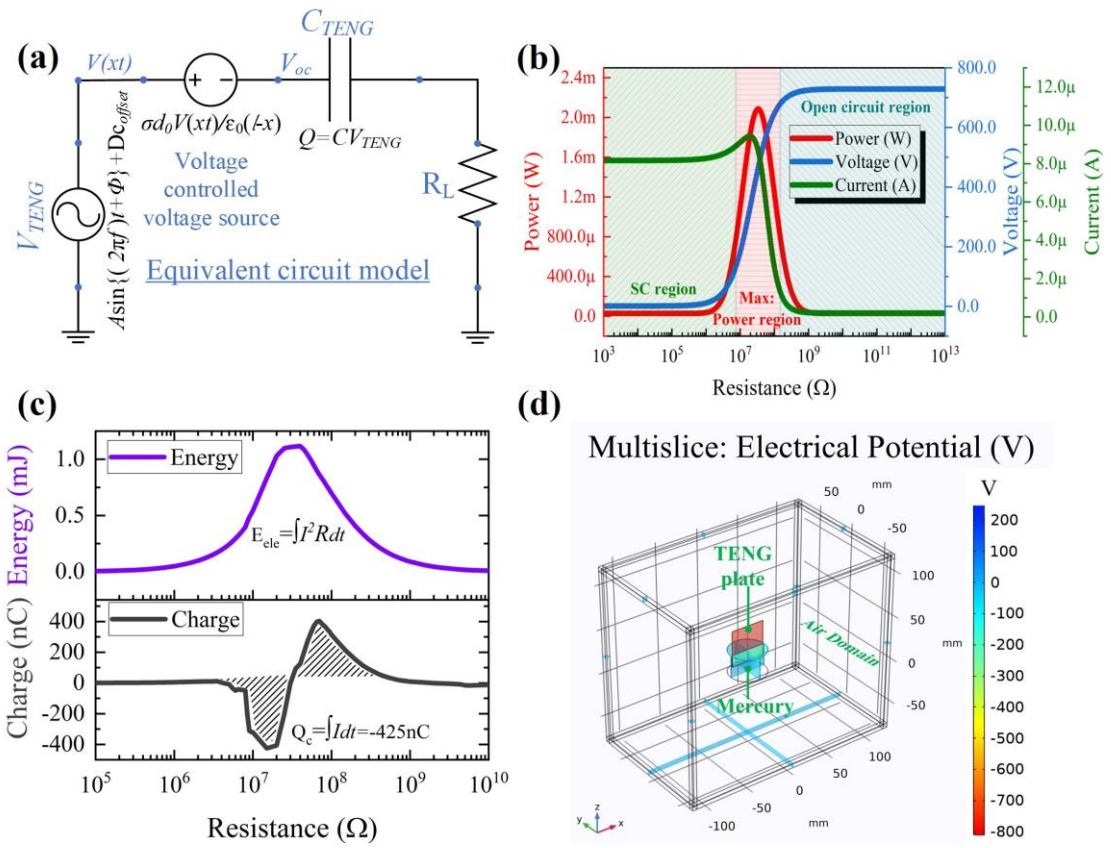

(a) Schematic of LM-TEG's equivalent circuit model. (**b)** Current, voltage, and power output of the LM-TEG at varying resistances. (**c)** LM-TEG's charge transfer and electrical energy output as predicted by the equivalent circuit model. (**d)** COMSOL FEM simulation of the TEG sliding in the mercury liquid metal.

3.2 Experimental results of the LM-TEG characteristics

In the initial stage of our experiment, we first devised a standalone system wherein a DC motor drives an LM-TEG to assess and optimize the performance of the LM-TEG. Fig. 3a demonstrates the experimental setup of the standalone LM-TEG driven by a DC motor. The Cu (electrode)- FEP (dielectric) films together make up the TEG part, which is driven by a DC motor, creating a reciprocating motion for the TEG to continuously immerse in and separate from the mercury (i.e., a liquid metal). Thus, an electric current is produced using the working principle explained in the previous section.

The electrical characteristics of the LM-TEG were assessed at a sliding velocity of 0.5 m/s. The dielectric material, induction electrode, and liquid metal are represented by FEP (with a thickness of 50 μm), copper (0.20 mm thick), and mercury, respectively. The outcomes of this measurement, including the short-circuit (SC) current as well as currents at 100 MΩ, and 1 GΩ resistances, are presented in Fig. 3b. Notably, the LM-TEG generated a maximum current amplitude of 17.6 μA in short circuit condition and 5.05 μA and 0.8 μA at 100 MΩ and 1 GΩ resistances, respectively. As illustrated in Fig. 3c, a total of 1.2 μC charge is produced in the SC condition, considering the contact area of 30 cm^2 (3×5 cm^2 each side), the output charge density reached an impressive 400 $\mu C/m^2$, significantly surpassing the charge density achieved by previous solid-to-solid contact methods, which typically hovered around 100 $\mu C/m^2$. Furthermore, the output current was examined under various load resistances, revealing stability when resistance remained below 100 MΩ. However, beyond that current gradually decreased indicating an optimal resistance value. The highest output power of approx. 5 mW (equivalent to a power density of 1.7 W/m^2) was achieved at a resistance of 100 MΩ and 1m/s velocity. In contrast, the equivalent circuit model we discussed earlier predicted a power density of 1.5 W/m^2. This is when the contact area is half its size (15 cm^2) and the velocity is a quarter of its maximum speed (0.25 m/s).

TEG's theory implicitly suggests that a larger contact area between mercury and TEG guarantees a higher performance. Intuitively, it is understood that a larger contact area involves a high charge transfer between the TEG and liquid metal interfaces. To validate this, we conducted experiments with varying widths of TEG plates in LM-TEG. Fig. 3d shows the current output of the 3 cm and 6 cm wide TEG plates at varying load resistances. By doubling the width from 3 cm to 6 cm, the contact area doubles while the length of the plate is kept the same. Fig. 3d confirms that the output current nearly doubles from 8.25 μA to 16.25 μA as the contact area of LM-TEG is doubled. Thus, it is verified that increasing contact area proportionally increases the performance of LM-TEG. Notice also the influence of dielectric film thickness on the LM-TEG performance indicating that the 80 μm thick FEP film performed best for the 3 cm wide TEG plate, whereas 50 μm thick FEP film performed optimally for the 6 cm wide TEG plate; all, at the short circuit condition (i.e., resistances, R=0), 100 MΩ, and 1 GΩ resistances.

Recall that the TEG part in LM-TEG includes two different materials, including an electrode (usually copper) and a friction (dielectric) material. A wide range of

materials can be used as a dielectric material for the TEG part; the most common include Kapton, FEP, and PET (Polyethylene terephthalate). Subsequently, we tested the three materials to assess and compare their performances. Fig. 3e illustrates the current output with different thicknesses of the Kapton, FEP, and PET dielectric films. All TEG plates are (3×10) cm^2 in area, and each plate's contact area (with the mercury) is set to half the plate length (3×5 cm^2 contact area on each side) at 30 cm^2. Fig. 3e shows that in all conditions, including short circuit condition (i.e., R=0), 100MΩ, and 1GΩ, FEP material exhibits a better performance than the Kapton and PET. Furthermore, it can be observed that the thickness of the dielectric materials significantly influences the TEG performance, indicating that the 80μm FEP film showed the overall best performance. We also tested the same dielectric materials with higher thickness, and it was observed that the performance decreased proportionally with the increase in the dielectric materials' thickness. This is because the induction distance increases with the increase in material thickness, negatively affecting the charge density. Finally, it was concluded that the FEP material is most suitable for LM-TEG and was thereupon chosen as an optimal material for all the experiments.

Note that in several experiments, we observed that both 50μm and 80μm demonstrated an overall better and stable performance. Realizing this, most experiments were conducted with either of these thicknesses. It is important to mention that literature on TEG research suggests that the thinner the dielectric material, the better the performance [43]. However, in our exhaustive and repeated LM-TEG experiments, after testing a range of thicknesses as low as 10 μm, we noticed that the performance of LM-TEG became unstable (i.e., ephemeral performance) for dielectric thicknesses below 50 μm. This instability was attributed to the mechanical limitations of extremely thin dielectric materials when immersed in dense mercury, leading to susceptibility to deformation, wear, or damage during operation. Additionally, thin dielectric materials' sensitivity to environmental conditions and non-uniform electric field distribution may have led to fluctuations in LM-TEG performance, affecting output power stability.

LM-TEG operates on the triboelectric effect, which involves the transfer of electric charges between the liquid metal and TEG when they come into contact and then separate. The rate at which the two surfaces separate (i.e., the velocity of relative motion) plays a crucial role. When the surfaces separate faster, the contact time is reduced, causing less charge recombination and more efficient charge transfer. This

results in a higher density of separated charges and an increased potential difference between the surfaces. In an acoustically driven system, velocity/frequency is critical for the system's performance; thus, it is imperative to experimentally investigate the velocity influence on LM-TEG's performance. Fig. 3f, g, h, respectively show the output current, power, and voltage at the varying velocity of LM-TEG with a 30 cm^2 contact area. It can be observed that in a short circuit (i.e., R=0) condition, the current increases proportionally with the increase in velocity, reaching a maximum value of 30 μA at a velocity of 2.4 m/s. However, in the presence of 100 MΩ and 1 GΩ load resistances, both current and power output increase correspondingly until an optimal velocity value of approx. 1m/s therein power reaches an optimal (saturation) value of approx. 5 mW (equivalent to a power density of 1.7 W/m^2). Conversely, further increasing the velocity beyond optimal value reduces both current and power. A similar trend is observed in the output voltage of the LM-TEG wherein, initially increases linearly with the velocity, reaching a maximum value of 759 V. The voltage output then decreases as the load resistance is further increased. This is conceivably, because, at velocities beyond optimal value, the mercury droplets at a high (separation and contact) rate don't have enough time to fully separate from the TEG surface and thus get built up at TEG's surface, negatively affecting the charge transfer between the two interfaces. Another possible reason may have to do with the rapid loss of charges with resistance due to voltage breakdown in air at higher velocities.

The output voltage and current of LM-TEG are influenced by the total resistance in its circuit. According to Ohm's law ($V = IR$), higher resistance can lead to a drop in output voltage for a given current or limit the current that can flow through the circuit for a given voltage. Likewise, power generated by an LM-TEG is the product of its voltage and current ($P = VI$). Higher resistance not only reduces current but also affects the voltage across the load, leading to a significant reduction in power output. To maximize power output, an optimal resistance value should be chosen. Hence, resistance plays a vital role in the performance of an LM-TEG by affecting the generated current, power output, and overall efficiency. Fig. 3i shows the influence of resistance on the current and power output of the LM-TEG at a velocity of 0.33 m/s. A maximum of 9 μA current is produced in short circuit conditions (i.e., R=0), which decreases as the resistance is increased. Moreover, the output power initially rises linearly as the resistance is increased, reaching an optimal value of approx. 2 mW at a 200 MΩ resistance, further increasing the resistance decreased the power output.

Hence, finding an optimal resistance is crucial to LM-TEG's output power and efficiency.

So far, the experiments have been conducted with a standalone TEG. One potential way to improve the performance of LM-TEG is by parallel stacking of multiple TEG plates. Tests were conducted by stacking multiple numbers of TEG plates in a 3D-printed Teflon holder (see Fig. S2 in the supplementary information file). Each plate has a contact area of 30 cm^2 and uses FEP dielectric material of 50 μm thickness and Cu electrode of 0.20 mm thickness. Fig. 3j shows the power output of the 10, 5, 4, 3, and 2 plate stacks at varying load resistance, indicating that power output increases corresponding with the increase in plate numbers. Notice that ten plates stack produced a maximum current of 95 μA at a resistance of 1 MΩ and power of approx. 35 mW at 10 MΩ optimal resistance. One significance of the results in Fig. 3j is that it provides an estimate of the current and power contributed by each plate in the stack, at a velocity of approx. 0.65m/s, each plate in the stack adds at least 10 μA and 3mW of current and power output, respectively. Considering a contact area of 30 cm^2, power and current densities of 1 W/m^2 and 3.3 mA/m^2 are deduced. Whereas, at 1m/s velocity, LM-TEG is estimated to provide a power density of 1.7 W/m^2. These results affirm a significant improvement over the typical milliwatt-scale power densities reported for conventional solid-solid contact TEGs. Importantly, the modular and scalable nature of the LM-TEG design allows for parallel stacking of multiple TEG plates to enable large-scale power production in heat-driven acoustic power generators.

Fig. 3: Experimental results of standalone Liquid metal triboelectric generator (LM-TEG)

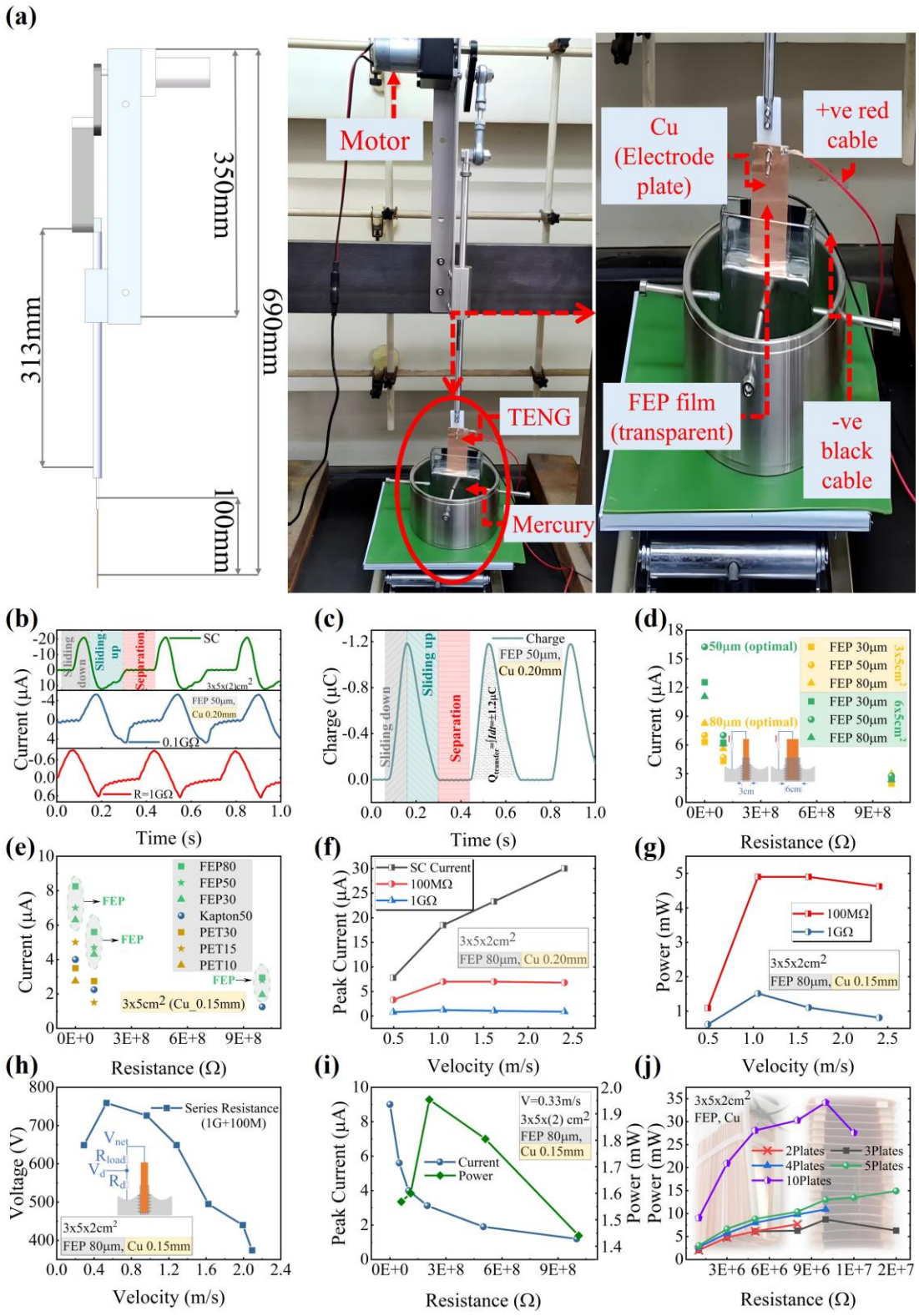

(a) Experimental Setup of standalone DC-motor driven LM-TEG. **(b)** TEG charge transfer over a cycle. **(c)** Time-varied current outputs at R=0 (short circuit), 100MΩ,

and 1GΩ of standalone DC-motor driven LM-TEG. (**d)** Influence of contact area on LM-TEG current at varying resistances. (**e)** Influence of dielectric material selection on LM-TEG's current at varying resistances. (**f)-(h)** Influence of velocity on LM-TEG (**f)** current, **(g)** power, and **(h)** voltage at varying resistances. (**i)** Effect of external resistance on LM-TEG's current and power. (**j)** Output power of parallelly stacked TEGs at varying resistances.

3.3 Experimenting with the LM-TEG in a high-pressure gas chamber

Until now, the LM-TEG experiments have been conducted in atmospheric conditions. In an acoustically driven LM-TEG setup, the system operates in a high-pressurized gas environment. Commonly used gases are helium, nitrogen, CO_2, etc. Subsequently, a high-pressure chamber was designed and built, as shown in Fig. 4a, to investigate the influence of gas type and gas pressure on the performance of LM-TEG. The DC motor-driven LM-TEG setup, illustrated in Fig. 3a in the previous section, is affixed inside a high-pressure chamber as shown in Fig. 4a, b. Illustrated in Fig. 4c is the influence of velocity on LM-TEG's performance when the chamber is filled with distinct gases at 1.5 MPa mean pressure. The LM-TEG setup uses a TEG plate of 3×5×(2sides) cm^2 contact area with FEP and Cu materials thicknesses of 80 μm and 0.20 mm, respectively. Results show that by merely switching from Helium to CO_2 gas, the LM-TEG's output current approximately doubled from 8.5 μA to 18 μA, indicating a significant influence of gas type on the LM-TEG's performance. Similarly, with CO_2 gas, the output current increased by approximately 1.5 times compared with air (under atmospheric conditions). Moreover, the LM-TEG's output current with CO_2 is marginally higher than in the SF_6 environment.

Owing to the maximum performance of CO_2 gas, experiments were also conducted at varying velocities and mean pressure to investigate their influence on the LM-TEG performance. Fig. 4d demonstrated the effect of velocity in a high-pressure environment (i.e., 1 MPa). In the short-circuit condition (i.e., R=0), the current increases linearly with velocity, reaching a maximum value of 18 μA at a velocity of 0.83 m/s. When subjected to load resistances of 100 MΩ and 1 GΩ, the current also increases linearly with velocity reaching a maximum value of 7.5 μA (at 100 MΩ) corresponding to a power output of 5.7 mW. Fig. 4e, f, respectively, display the current and power output produced at varying mean pressure and resistance. At a CO_2 charge pressure of 1 MPa

and a velocity of 0.43 m/s, the LM-TEG had a maximum short-circuit current of 13.25 μA and a power of 3.2 mW at a resistance of 100 MΩ.

These results signify the influence of gas type, pressure, and velocity on the performance of LM-TEG operating in a high-pressure environment. The notable increase in output current under CO_2 suggests its potential as a preferred gas medium for optimizing LM-TEG performance in practical applications. Furthermore, it can be deduced with caution that compared to the air, LM-TEG performed better in heavier gas environments. Higher gas densities and pressures can result in more frequent collisions and interactions, potentially enhancing charge generation and transfer mechanisms within the LM-TEG. Additionally, the difference is also due to the differences in the dielectric strength of different gases. Dielectric strength $(E/P)_{critical}$ is the ratio of electric field strength (E) and gas pressure (P). A higher dielectric strength is desirable, indicating ionization is less likely to occur (i.e., the ionization potential of a gas refers to the energy required to remove an electron from an atom or molecule, thereby forming ions. Gases with lower ionization potentials may facilitate electron transfer processes more readily, leading to increased charge generation and output current in the LM-TEG). Since CO_2 and SF_6 have higher dielectric strength and lower ionization potential, their performance is better than air, which, in the case of helium, are opposite compared to air; hence, the performance is lacking. Note that based on our explanation, LM-TEG in the SF_6 gas environment should have performed better than CO_2. Our understanding is that despite SF_6 gas's high density and excellent dielectric strength, its high susceptibility to react with moisture may have compromised its dielectric strength [44], [45] resulting in deteriorating LM-TEG's performance.

Similar experiments were also conducted with the nitrogen and argon gases. These experiments conclude that the performance of LM-TEG is enhanced in a high-pressure environment. Furthermore, compared to the air, LM-TEG performed better in N_2 environments. However, in the Argon environment, the LM-TEG's performance was less than in the atmospheric conditions (air).

Fig. 4: Experimental results of the standalone LM-TEG in a high-pressure chamber.

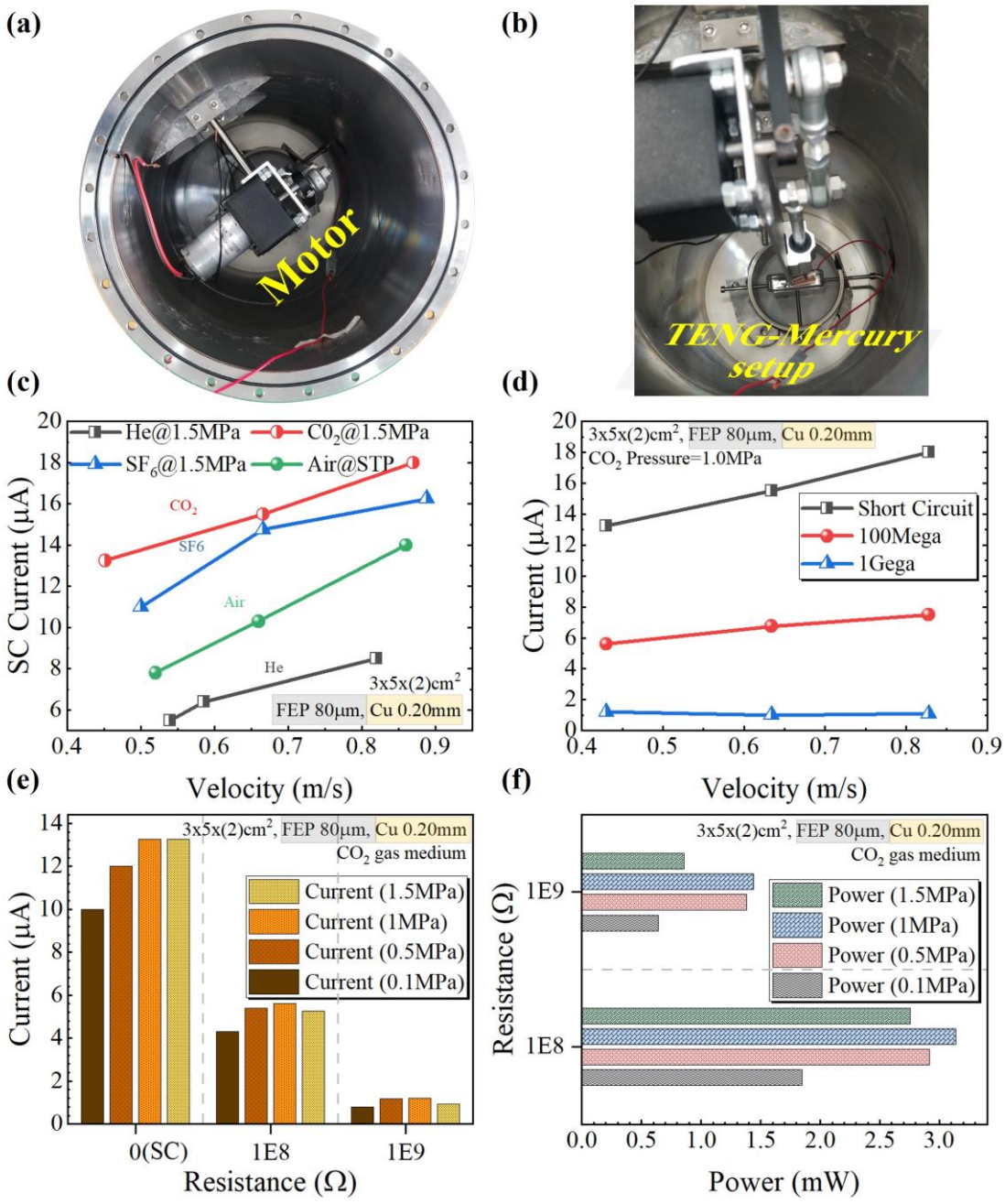

(a), (b) DC-motor driven LM-TEG setup fastened inside the high-pressure chamber. **(c)** Effect of gas selection at high pressure on LMTEG's performance. **(d)** Influence of velocity on LM-TEG current at 1MPa pressure of CO_2 gas. **(e), (f)** Effect of mean pressure on current and power output at varying resistance

3.4 Acoustically driven Liquid Metal-Triboelectric Generator (LM-TEG)

The standalone LM-TEG and high-pressure chamber experiments provided valuable understanding and insight into the LM-TEG operation and characteristics. Following this, a logical forward step was to experiment with the acoustically driven LM-TEG. Subsequently, an LM-TEG driven by a linear motor is fabricated, as shown in Fig. 5a. The setup was first designed and optimized using the Sage [46] modeling software; later, a physical model of the system was developed in SolidWorks. (See Fig. S3 in the supplementary information file). The experimental setup in Fig. 5a has three distinct sections: a driving system including a dual-opposed linear motor, a resonator section, and an LM-TEG section including a U-shaped pipe, a vertical duct housing a TEG plate, and a gas backflow chamber. Notice in Fig. 5a that a combination of two distinct materials, steel and polyether ether ketone (aka peek-beige-colored parts), are used in the system to make it lightweight and cost-effective. The U-shaped part contains approx. 4 kg of mercury and exhibits a 30 cm^2 contact area with the TEG plate. The TEG plate itself measures 3x5 cm^2 with FEP and Cu materials thicknesses of 80 μm and 0.20 mm, respectively, and is housed in the vertical peek section. Pressurized gas was charged from two sides of mercury; notice the two gas valve locations in Fig. 5a. The current and voltage output of the LM-TEG were measured using the methodology described in the methods section. At first, helium gas at 1MPa pressure was charged into the acoustically driven system, and the resonance of the system was achieved at 1.5Hz.

Fig. 5b shows that at a pressure of 1 MPa with helium as the working gas, the system produced approx. 1.5 μA current in short circuit condition. In Fig. 5b, the blue highlighted area represents the part when the mercury in a U-shaped tube is sliding up and in contact with the TEG plate. In contrast, the grey area highlights the part of the cycle when the mercury slides back to the U-shaped tube due to the effect of gravity and gas backflow. The mercury in the system essentially operates akin to an unconstrained piston.

The high-pressure experiments in the previous section concluded that the LM-TEG's performance improves in heavier gas environments. Specifically, the CO_2 gas enabled the highest performance. However, in the acoustically driven LM-TEG experiments, the high density of CO_2 gas caused the system's resonance frequency to drop significantly (>1 Hz), making it impractical. Consequently, the system was instead tested using N_2 gas, which was found to be the next best option. Nitrogen has a higher

dielectric strength value compared to helium, and while not quite as effective as CO_2 at suppressing breakdown, the N_2 gas environment still enabled significant performance improvements.

To validate this, the acoustically driven system was charged with N_2 gas at a mean pressure of 1 MPa. Fig. 5c shows the pressure variation and the short circuit current produced by the system with N_2 as the working gas. A maximum current of 7 μA is produced, which is 4.5 times higher than the current generated with the helium gas.

To further substantiate the charge density capabilities of the LM-TEG compared to its solid-solid counterpart, a charge production assessment was conducted within the acoustically driven system. Fig. 5d, e respectively, capture the temporal analysis of the LM-TEG's performance in the He and N_2 gas environment. This graph visualizes time on the x-axis and presents two parameters on the y-axis. The left y-axis shows charge amplitude while the right y-axis demonstrates the corresponding pressure variations experienced within the (He and N_2-filled) acoustic system, charged at a pressure of 1 MPa. During the experiment, the LM-TEG achieved a peak charge production of 0.12 μC in He and 1.165 μC in the N_2 gas environment. Considering the LM-TEG's contact area of 30 cm^2 (i.e., with a single TEG plate) and 1.165 μC of charge in an N_2 gas environment translates to a charge density of approximately 388 $\mu C/m^2$. This charge density surpasses the typical 100 $\mu C/m^2$ threshold observed in conventional solid-solid contact TEGs [35], [36]. The difference in charge density highlights the LM-TEG's superiority in generating and accumulating electrical charge for energy harvesting applications.

Preliminary experimental results show that LM-TEG has considerably less power density than the traditionally used alternators ($<100 W/m^2$) for acoustic-to-electric conversion in heat-driven acoustic power generators. However, LM-TEGs offer an innovative approach to energy harvesting, addressing specific challenges and complementing traditional generators in scenarios where conventional solutions fall short. Choosing an LM-TEG for acoustic-to-electric conversion within a HDAE provides several distinct advantages. LM-TEGs efficiently convert low-frequency vibrations, which align with the typical acoustic wave frequencies generated by heat-driven acoustic power generators. Unlike alternators, LM-TEGs operate without the need for rotational motion. This unique characteristic allows the coupling of a heat-driven acoustic power generator and TEG to yield an engine without any mechanical

Fig. 5: Experimental setup and results of the Acoustically driven Liquid Metal-Triboelectric Generator (LM-TEG).

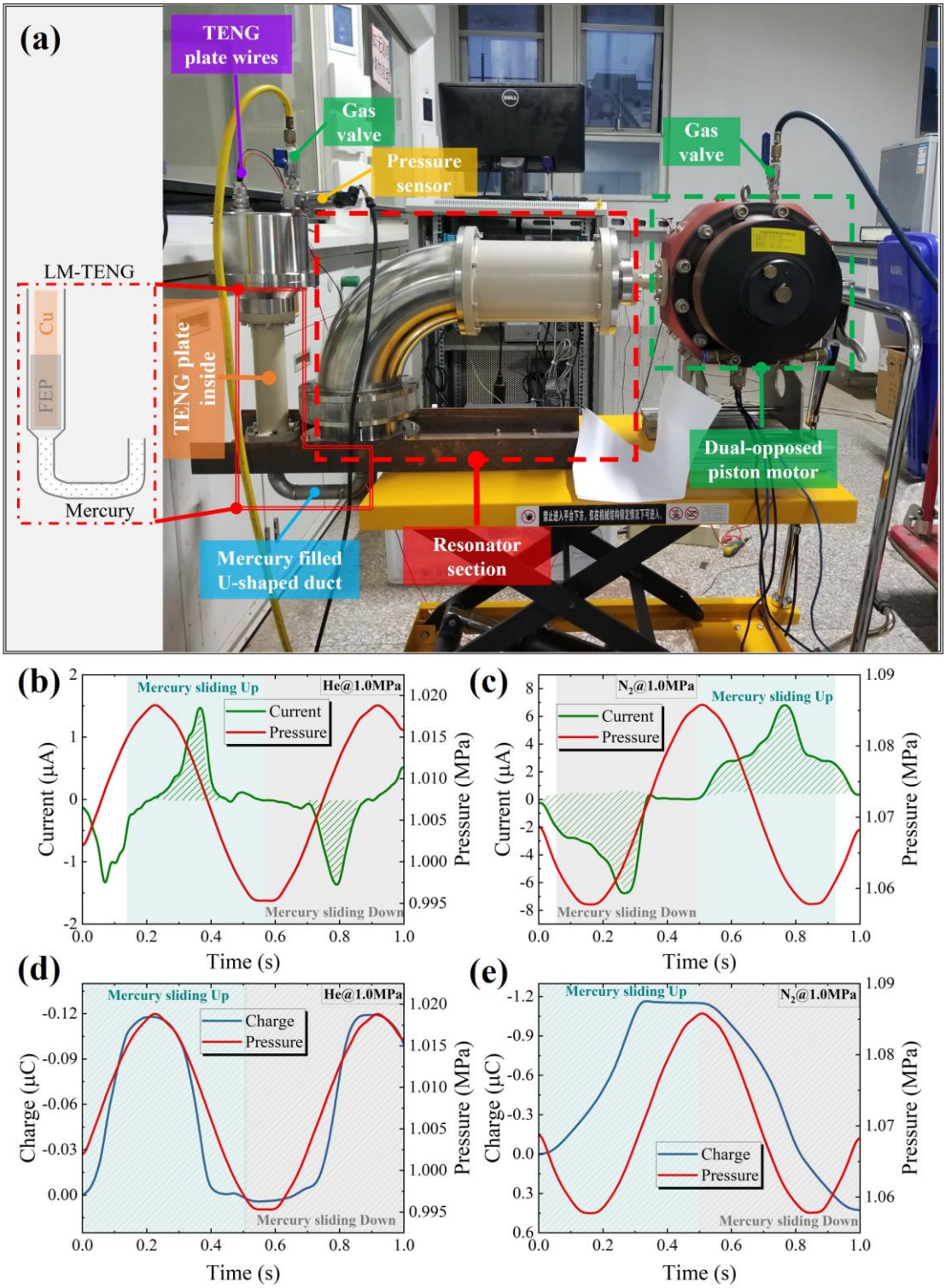

(a) Experimental setup of the acoustically driven LM-TEG driven by dual opposed piston linear motor. **(b)**, **(c)** Pressure variations and current produced by the acoustically

driven system with Helium and N_2 at 1 MPa pressure. **(d)**, **(e)** Electric charge produced by the acoustically driven LM-TEG system with Helium and N_2 at 1 MPa pressure.

components. TEGs exhibit heightened sensitivity to low-frequency and low-amplitude vibrations, capturing energy from even the subtle waves produced by the engine. Additionally, TEGs offer a simpler design, which can be beneficial in terms of ease of implementation and contrast with alternators that involve mechanical components requiring high cost and maintenance. Overall, LM-TEG is a promising choice for various niche applications in a heat-driven acoustic power generator for converting acoustic energy into electricity.

4. Discussion and Conclusions

This paper introduced a groundbreaking concept for an acoustic-to-electrical power generator devoid of any solid moving components, presenting a prototype as proof of its feasibility. This innovative generator holds the promise of an extended operational lifespan and boasts a high theoretical acoustic-to-electric conversion efficiency. Three distinct sets of experiments were conducted, involving the experiments of mechanically driven LM-TEG in an atmospheric environment, LM-TEG in a pressurized gas chamber, and an acoustically driven LM-TEG. The findings from the experiments involving mechanically driven Liquid Metal Triboelectric Generators (LM-TEGs) suggest that the utilization of FEP material, a large contact area between the LM-TEGs, parallel arrangement of multiple TEGs, and a pressurized gas environment all contribute to improved power generation. LM-TEG with mercury liquid metal, FEP as dielectric, and Cu electrode materials with thicknesses of 80 μm and 0.2 mm, respectively exhibited a maximum power density of 1.7 W/m^2. Furthermore, preliminary experiments with the acoustically driven LM-TEG prototype have successfully demonstrated the concept, achieving a short-circuit current of 7 μA and 388 $\mu C/m^2$ charge density.

To conclude, the heat-driven acoustic generator driven liquid metal TEG represents an innovative thermal power generator that distinguishes itself by its capacity to transform thermal energy into electrical power without relying on any solid moving components.

Acknowledgments

This work was supported in part by the National Natural Science Foundation projects of China (NSFC no. 51876214 and no. 52306031). We extend gratitude to Mr. Chengyu Li for his assistance in fabricating Triboelectric Generators (TEGs). The specific equipment, instruments, and materials used in this study are identified to ensure that the experimental procedures can be adequately replicated. This identification is not intended as a recommendation or endorsement of these particular items, nor does it imply that they are necessarily the optimal choices available for the given purpose.

References

[1] IRENA, World Energy Transitions Outlook 2023, Abu Dhabi, 2023.

[2] P. IEA, World Energy Outlook 2022, Paris, 2022.

[3] S. Zhu, G. Yu, K. Liang, W. Dai, E. Luo, A review of Stirling-engine-based combined heat and power technology, Appl. Energy 294 (2021) 116965. https://doi.org/10.1016/J.APENERGY.2021.116965.

[4] G.W. Swift, Thermoacoustics: A Unifying perspective for some engines and refrigerators: Second edition, 2017. https://doi.org/10.1007/978-3-319-66933-5.

[5] S. Backhaus, G.W. Swift, A thermoacoustic Stirling heat engine, Nat. 1999 3996734 399 (1999) 335–338. https://doi.org/10.1038/20624.

[6] M.E.H. Tijani, S. Spoelstra, A high performance thermoacoustic engine, J. Appl. Phys. 110 (2011). https://doi.org/10.1063/1.3658872.

[7] L. Guo, D. Zhao, L. Cheng, X. Dong, J. Xu, Enhancing energy conversion performances in standing-wave thermoacoustic engine with externally forcing periodic oscillations, Energy 292 (2024) 130634. https://doi.org/10.1016/j.energy.2024.130634.

[8] L. Guo, D. Zhao, G. Yu, X. Dong, Numerical investigations on energy conversion performances in twin standing-wave thermoacoustic engines with various geometric and operational conditions, Therm. Sci. Eng. Prog. 45 (2023) 102134. https://doi.org/10.1016/j.tsep.2023.102134.

[9] A. Maddi, C. Olivier, G. Poignand, G. Penelet, V. Pagneux, Y. Aurégan, Frozen sound: An ultra-low frequency and ultra-broadband non-reciprocal acoustic absorber, Nat. Commun. 14 (2023) 4028. https://doi.org/10.1038/s41467-023-39727-4.

[10] S. Backhaus, E. Tward, M. Petach, Traveling-wave thermoacoustic electric generator, Appl. Phys. Lett. 85 (2004) 1085–1087. https://doi.org/10.1063/1.1781739.

[11] T. Bi, Z. Wu, L. Zhang, G. Yu, E. Luo, W. Dai, Development of a 5 kW traveling-wave thermoacoustic electric generator, Appl. Energy 185 (2017) 1355–1361. https://doi.org/10.1016/j.apenergy.2015.12.034.

[12] M.A.G. Timmer, K. de Blok, T.H. van der Meer, Review on the conversion of thermoacoustic power into electricity, J. Acoust. Soc. Am. 143 (2018) 841–857. https://doi.org/10.1121/1.5023395.

[13] J. Smoker, M. Nouh, O. Aldraihem, A. Baz, Energy harvesting from a standing wave thermoacoustic-piezoelectric resonator, J. Appl. Phys. 111 (2012) 104901. https://doi.org/10.1063/1.4712630.

[14] F. Ahmed, G. Yu, E. Luo, Multi-method modeling to predict the onset conditions and resonance of the piezo coupled thermoacoustic engine, J. Acoust. Soc. Am. 151 (2022) 4180–4195. https://doi.org/10.1121/10.0011744.

[15] R.M. Keolian, J.W. Wuthrich, K.J. Bastyr, Thermacoustic piezoelectric generator, 7,772,746, 2010.

[16] S. Zhu, T. Wang, C. Jiang, Z. Wu, G. Yu, J. Hu, C.N. Markides, E. Luo, Experimental and numerical study of a liquid metal magnetohydrodynamic generator for thermoacoustic power generation, Appl. Energy 348 (2023) 121453. https://doi.org/10.1016/j.apenergy.2023.121453.

[17] S. Zhu, G. Yu, C. Jiang, T. Wang, L. Zhang, Z. Wu, J. Hu, C.N. Markides, E. Luo, A novel thermoacoustically-driven liquid metal magnetohydrodynamic generator for future space power applications, Energy Convers. Manag. 258 (2022) 115503. https://doi.org/10.1016/J.ENCONMAN.2022.115503.

[18] A. Alemany, A. Krauze, M. Al Radi, Thermo acoustic - MHD electrical generator, Energy Procedia 6 (2011) 92–100. https://doi.org/10.1016/j.egypro.2011.05.011.

[19] H. Wu, S. Wang, Z. Wang, Y. Zi, Achieving ultrahigh instantaneous power density of 10 MW/m2 by leveraging the opposite-charge-enhanced transistor-like triboelectric nanogenerator (OCT-TENG), Nat. Commun. 12 (2021) 5470. https://doi.org/10.1038/s41467-021-25753-7.

[20] Y. Xie, S. Wang, S. Niu, L. Lin, Q. Jing, J. Yang, Z. Wu, Z. Lin Wang, Y. Xie, S. Wang, S. Niu, L. Lin, Q. Jing, J. Yang, Z.L. Wang, Z. Wu, Grating-Structured Freestanding Triboelectric-Layer Nanogenerator for Harvesting Mechanical Energy at 85% Total Conversion Efficiency, Adv. Mater. 26 (2014) 6599–6607. https://doi.org/10.1002/ADMA.201402428.

[21] M. Yuan, C. Li, H. Liu, Q. Xu, Y. Xie, A 3D-printed acoustic triboelectric nanogenerator for quarter-wavelength acoustic energy harvesting and self-powered edge sensing, Nano Energy 85 (2021) 105962. https://doi.org/10.1016/J.NANOEN.2021.105962.

[22] C. Chen, Z. Wen, J. Shi, X. Jian, P. Li, J.T.W. Yeow, X. Sun, Micro triboelectric ultrasonic device for acoustic energy transfer and signal communication, Nat. Commun. 2020 111 11 (2020) 1–9. https://doi.org/10.1038/s41467-020-17842-

w.

[23] Z.L. Wang, Triboelectric Nanogenerators as New Energy Technology for Self-Powered Systems and as Active Mechanical and Chemical Sensors, ACS Nano 7 (2013) 9533–9557. https://doi.org/10.1021/nn404614z.

[24] F.R. Fan, Z.Q. Tian, Z. Lin Wang, Flexible triboelectric generator, Nano Energy 1 (2012) 328–334. https://doi.org/10.1016/j.nanoen.2012.01.004.

[25] Z.L. Wang, Triboelectric Nanogenerator (TENG)—Sparking an Energy and Sensor Revolution, Adv. Energy Mater. 10 (2020) 2000137. https://doi.org/10.1002/AENM.202000137.

[26] T. Cheng, J. Shao, Z.L. Wang, Triboelectric nanogenerators, Nat. Rev. Methods Prim. 2023 31 3 (2023) 1–13. https://doi.org/10.1038/s43586-023-00220-3.

[27] Z.L. Wang, On the first principle theory of nanogenerators from Maxwell's equations, Nano Energy 68 (2020) 104272. https://doi.org/10.1016/j.nanoen.2019.104272.

[28] S. Niu, Y.S. Zhou, S. Wang, Y. Liu, L. Lin, Y. Bando, Z.L. Wang, Simulation method for optimizing the performance of an integrated triboelectric nanogenerator energy harvesting system, Nano Energy 8 (2014) 150–156. https://doi.org/10.1016/j.nanoen.2014.05.018.

[29] S. Niu, Y. Liu, S. Wang, L. Lin, Y.S. Zhou, Y. Hu, Z.L. Wang, Theory of Sliding-Mode Triboelectric Nanogenerators, Adv. Mater. 25 (2013) 6184–6193. https://doi.org/10.1002/adma.201302808.

[30] S. Niu, Y. Liu, X. Chen, S. Wang, Y.S. Zhou, L. Lin, Y. Xie, Z.L. Wang, Theory of freestanding triboelectric-layer-based nanogenerators, Nano Energy 12 (2015) 760–774. https://doi.org/10.1016/J.NANOEN.2015.01.013.

[31] S. Niu, Y. Liu, S. Wang, L. Lin, Y.S. Zhou, Y. Hu, Z.L. Wang, Theoretical Investigation and Structural Optimization of Single-Electrode Triboelectric Nanogenerators, Adv. Funct. Mater. 24 (2014) 3332–3340. https://doi.org/10.1002/ADFM.201303799.

[32] F. Ahmed, G. Yu, E. Luo, A triboelectric nanogenerator attached to a thermoacoustic heat engine for power generation, Energy Convers. Manag. 276 (2023) 116482. https://doi.org/10.1016/j.enconman.2022.116482.

[33] S. Zhu, A. Yu, G. Yu, Y. Liu, J. Zhai, W. Dai, E. Luo, Thermoacoustically driven triboelectric nanogenerator: Combining thermoacoustics and nanoscience, Appl. Phys. Lett. 111 (2017) 153901. https://doi.org/10.1063/1.4999284.

[34] W. Tang, T. Jiang, F.R. Fan, A.F. Yu, C. Zhang, X. Cao, Z.L. Wang, Liquid-Metal Electrode for High-Performance Triboelectric Nanogenerator at an Instantaneous Energy Conversion Efficiency of 70.6%, Adv. Funct. Mater. 25 (2015) 3718–3725. https://doi.org/10.1002/adfm.201501331.

[35] L. Lin, S. Wang, Y. Xie, Q. Jing, S. Niu, Y. Hu, Z.L. Wang, Segmentally Structured Disk Triboelectric Nanogenerator for Harvesting Rotational Mechanical Energy, Nano Lett. 13 (2013) 2916–2923. https://doi.org/10.1021/nl4013002.

[36] W. Du, X. Han, L. Lin, M. Chen, X. Li, C. Pan, Z.L. Wang, A Three Dimensional Multi-Layered Sliding Triboelectric Nanogenerator, Adv. Energy Mater. 4 (2014) 1301592. https://doi.org/10.1002/aenm.201301592.

[37] Y. Zi, S. Niu, J. Wang, Z. Wen, W. Tang, Z.L. Wang, Standards and figure-of-merits for quantifying the performance of triboelectric nanogenerators, Nat. Commun. 6 (2015) 8376. https://doi.org/10.1038/ncomms9376.

[38] L. Cheng, Q. Xu, Y. Zheng, X. Jia, Y. Qin, A self-improving triboelectric nanogenerator with improved charge density and increased charge accumulation speed, Nat. Commun. 9 (2018) 3773. https://doi.org/10.1038/s41467-018-06045-z.

[39] W. Liu, Z. Wang, G. Wang, Q. Zeng, W. He, L. Liu, X. Wang, Y. Xi, H. Guo, C. Hu, Z.L. Wang, Switched-capacitor-convertors based on fractal design for output power management of triboelectric nanogenerator, Nat. Commun. 11 (2020) 1883. https://doi.org/10.1038/s41467-020-15373-y.

[40] H. Zou, L. Guo, H. Xue, Y. Zhang, X. Shen, X. Liu, P. Wang, X. He, G. Dai, P. Jiang, H. Zheng, B. Zhang, C. Xu, Z.L. Wang, Quantifying and understanding the triboelectric series of inorganic non-metallic materials, Nat. Commun. 11 (2020) 2093. https://doi.org/10.1038/s41467-020-15926-1.

[41] S. Zhu, G. Yu, W. Tang, J. Hu, E. Luo, Thermoacoustically driven liquid-metal-based triboelectric nanogenerator: A thermal power generator without solid moving parts, Appl. Phys. Lett. 118 (2021). https://doi.org/10.1063/5.0041415.

[42] K. Tang, T. Lei, T. Jin, X.G. Lin, Z.Z. Xu, A standing-wave thermoacoustic engine with gas-liquid coupling oscillation, Appl. Phys. Lett. 94 (2009). https://doi.org/10.1063/1.3157920.

[43] S. Niu, S. Wang, Y. Liu, Y.S. Zhou, L. Lin, Y. Hu, K.C. Pradel, Z.L. Wang, A theoretical study of grating structured triboelectric nanogenerators, Energy

Environ. Sci. 7 (2014) 2339–2349. https://doi.org/10.1039/C4EE00498A.

[44] R. Bell, R. Hicksted, J. VanVliet, M. Bertin, SF^6 Dielectric Fill Gas Gauge, California, 1978.

[45] M.-C. Lessard, G. Larocque, S. Gendron, S. Laberge, Y. Lavoie, A new approach for assessing the moisture content in SF^6-insulated equipment, in: 2016 IEEE Electr. Insul. Conf., IEEE, 2016: pp. 539–542. https://doi.org/10.1109/EIC.2016.7548659.

[46] D. Gedeon, Sage User's Guide, Athens, OH 45701, 2016.